Evaporation-induced self-assembly synthesis of Ni-doped mesoporous SnO_2 thin films with tunable room temperature magnetic properties

Jungpeng Fan[a], Miguel Guerrero[a,*], Adrián Carretero-Genevrier[b], Maria Dolors Baró[a], Santiago Suriñach[a], Eva Pellicer[a,*], J. Sort[a,c]

[a]Departament de Física, Facultat de Ciències, Universitat Autònoma de Barcelona, E-08193 Bellaterra, Cerdanyola del Vallès, Barcelona, Spain.

[b]Institut d’Electronique et des Systemes (IES), CNRS, Universite Montpellier 2 860 Rue de Saint Priest 34095 Montpellier, France.

[c]Institució Catalana de Recerca i Estudis Avançats (ICREA), Pg. Lluís Companys 23, E-08010 Barcelona, Spain

Abstract

Mesoporous Ni-doped SnO_2 thin films synthesized from variable [Ni(II)/Sn(IV)] molar ratios (0:100, 5:95, 10:90, 15:85 and 20:80), thickness in the range of 100-150 nm, and average pore size lower than 10 nm were obtained through a sol-gel based self-assembly process using Pluronic P-123 as structure-directing agent. Grazing incidence X-ray diffraction experiments indicate that the films mostly possess the tetragonal SnO_2 structure with Ni^{2+} in substitutional positions, although energy-dispersive X-ray analyses also reveal the occurrence of small NiO clusters in the films produced from high [Ni(II)/Sn(IV)] molar ratios (corresponding to a Ni amount of 8.6 at.%). X-ray photoelectron spectroscopy experiments indicate lack of metallic Ni and the occurrence of oxygen vacancies in the mesoporous films. Interestingly, the

magnetic properties of these mesoporous films significantly vary as a function of the doping percentage. The undoped SnO_2 films exhibit a diamagnetic behavior, whereas a clear paramagnetic signal dominates the magnetic response of the Ni-doped mesoporous films, probably due to the presence of NiO as secondary phase. A small ferromagnetic-like contribution superimposed to the paramagnetic background is observed for samples with high Ni contents, possibly stemming from the combined effect from Ni incorporation and the occurrence of oxygen vacancies.

***Corresponding authors:** Miguel.Guerrero@uab.cat, Eva.Pellicer@uab.cat

1. Introduction

Oxide semiconductors are among the most widely investigated materials in contemporary condensed matter physics and inorganic chemistry due to their wide range of technological applications in areas like energy conversion and storage, environmental remediation, light emission, magnetic and resistive memories or optoelectronic devices.[1-5] In recent years, the introduction of transition metals (TM) as doping atoms in the crystallographic structure of oxide semiconductors has emerged as a primary method to modify their electronic band configuration and, consequently, tailor some of their physical properties (e.g., electric conductivity, resistive switching behavior or magnetism), eventually leading to enhanced or even new functionalities.[5-7]

Many of the applications of semiconducting oxides (e.g., photocatalysis, gas sensors or electrochemical energy storage devices) take advantage from the use of materials with a large surface area-to-volume ratio. Hence, much progress is being made to develop new synthetic pathways to grow these materials in the form of nanoscale objects (e.g., nanowires or nanoparticles)[8,9] or as highly nanoporous frameworks (powders or films) with precise control of the degree of porosity, pore size and crystallinity of the pore walls.[10-12] Diverse strategies can be utilized to generate nanoporosity, by either removing material from the fully-dense counterpart by, e.g., chemical etching or ion irradiation (top-down approach), or assembling small building blocks in three-dimensions while leaving voids or empty spaces in-between (bottom-up approach).

For the synthesis of mesoporous (with pore size ranging between 2 to 50 nm) oxide powders, both soft and hard templating methods can be utilized.[13] Soft templating is mostly

used for, but not restricted to, the preparation of mesoporous silicates, mixed oxides, metallophosphates, organic–inorganic hybrids or mesoporous carbon powders.[14,15] It employs organic (soft) templates (surfactants and their supramolecular assemblies) as structure-directing agents during the chemical reaction to produce the nanoporous scaffolds. In turn, hard templating or nanocasting uses porous rigid templates (typically mesoporous silica or carbon) as molds to form nanoporous oxide semiconductors of interest, which constitute the negative replica of the parent template. This technique has emerged as perhaps the most cost-effective method to produce ordered nanoporous oxide powders with a precise control of the pore size in diverse geometrical architectures.[16]

However, many applications require of nanoporous films instead of powders. Tunable porosity can be achieved in metal oxide films by block-copolymer templating[17,18] or colloidal crystal templating followed by solution dipping. In the first case, well-defined microdomains of block copolymers with different etching sensitivities allow them to be used as nanolithographic resists. The latter consists of first assembling a monolayer (or multilayer) of polymeric spheres onto a substrate, then soaking the substrate into the precursor solution and finally performing calcinations to burn off the polymer and convert the precursor into the desired oxide.[19] Compared to the block-copolymer templating approach, though, the resulting pores are macroporous –typically beyond 200 nm, which correspond to the diameter of commercially available spheres. Alternatively, the so-called evaporation-induced self-assembly (EISA) method can be used to prepare oxide semiconductors and insulators in the form of nanoporous films (e.g., In_2O_3, ZnO, TiO_2, SiO_2, etc.).[20-22] EISA is based on the solution phase co-assembly of an inorganic precursor and the surfactant molecules to form hybrid intermediate entities. Films are first deposited by, for example, dip-coating onto polar

substrates and then withdrawn from the precursor solution at a constant rate under controlled humidity and temperature. Nanoporous films are obtained after cross-linking of the inorganic framework and simultaneous removal of the organic template by calcination. Pore sizes well below 50 nm are achieved.

Compared to mesoporous metal oxide powders, the literature dealing with the synthesis of thin film analogues is less abundant. This is particularly true for SnO_2, a paradigmatic transition metal oxide whose powder synthesis has been intensively pursued for chemoresistive gas sensing applications.[23,24]. Mesoporous SnO_2 films have been prepared by EISA and related sol-gel chemistry procedures accompanied with post-synthetic hydrothermal transformations.[25,26] The focus has been mainly on investigating the influence of the synthesis variables on the final characteristics of the thin film[27,28], or exploring their optical[29] and electrochemical properties.[30] A common feature of these works is the use of Pluronic F-127 polymer as structure-directing agent. Reports dealing with the synthesis of multimetallic or "doped" nanoporous SnO_2 films are more scarce,[30-32] in spite of the aforementioned interest of this type of materials.

While the magnetic properties of fully-dense oxide semiconductors are a topic of extensive research (i.e., the so-called oxide diluted magnetic semiconductors), the magnetic behavior of mesoporous TM-doped oxide films is generally not studied, as these materials are mainly synthesized for chemical or physicochemical purposes/applications. It is surprising that although many of the cutting-edge technological applications in magnetism and spintronics also rely on surface or interface magnetic phenomena, the use of nanoporous magnetic frameworks in these technologically-relevant fields has just emerged during the last few years.[33-38]

During the last few years, we have reported the synthesis and magnetic characterization of TM-doped oxide semiconducting mesoporous powders prepared by nanocasting.[35-37] The doping with the TM confers a magnetic character to this type of materials, which can then be categorized as mesoporous oxide-diluted magnetic semiconductors (MODMS). These mesoporous frameworks may be appealing for spintronic applications, where the spin of the electrons (and not only the electric charge) can be used for the processing of information. Additionally, MODMS could exhibit additional unique properties, as compared to their bulk counterparts, such as quantum-confinement effects, surface spin-glass or uncompensated spins, and combined optical and magnetic surface effects. Aside from their fundamental interest, in order to use this type of materials in real electronic devices, full assessment of the magnetic performance of MODMS *films instead of powders*, is required.

In this work, we report on the growth of mesoporous Ni-doped SnO_2 films by the EISA method, employing Pluronic P123 as structure-directing agent. A detailed structural characterization of the obtained materials, with emphasis on the role of Ni as doping TM, its distribution and speciation, is performed. We also examine the magnetic properties of the thin films and find out that the incorporation of Ni induces large variations in the magnetic susceptibility together with a small ferromagnetic-like contribution.

2. Experimental section

2.1 General remarks

Anhydrous tin (IV) chloride ($SnCl_4$, 99.995%), nickel (II) chloride ($NiCl_2$, 98%), absolute ethanol (CH_3CH_2OH, 99.8%) and Pluronic P-123 block copolymer

($HO(CH_2CH_2O)_{20}[CH_2CH(CH_3)O]_{70}(CH_2CH_2O)_{20}H$) were purchased from Sigma Aldrich and used as-received without further purification. Milli-Q water (≥ 18.2 MΩ·cm) was obtained through an EMD Millipore Simplicity™ Water Purification System (Millipore S.A.S., 67120 Molsheim, France). Silicon chips (1 × 3 cm^2) with {111} orientation were used as substrates for dip-coating.

2.2 Preparation of precursor solutions

P-123 (0.12 g) was dissolved in absolute ethanol (6 mL) by vigorous stirring (300 rpm/min) at room temperature. Next, $SnCl_4$ (0.55 g) and deionized water (0.4 mL) were added to the previous solution. The resulting mixture led to pure SnO_2 film (section 2.3), which was taken as a reference. For the Ni-doped SnO_2 films, precursor solutions containing [Ni(II)/Sn(IV)] molar ratios of 5:95, 10:90, 15:85 and 20:80 were targeted. To this end, different amounts of $NiCl_2$ (0.0144 g, 0.0304 g, 0.0483 g, 0.0684 g, respectively) were added to the Sn(IV) solution. Notice that the $SnCl_4$ concentration was kept constant in each synthesis. The resulting solutions were sealed and aged for 12 h at room temperature before deposition.

2.3 Fabrication of the thin films via EISA process

Prior to use, each Si substrate was cleaned with acetone and Milli-Q water in an ultrasonic bath for 5 min each, and then rinsed with absolute ethanol. The mesoporous films were prepared in an automatic dip coater (Coater 5 AC, ID LAB) at a withdrawal speed of 5 mm s^{-1} under a relative humidity of around 20 %. After deposition, the resulting coatings were dried under ambient atmosphere for 30 min and then put into the furnace to be calcined under air at 100 ℃ for 12 h (heating ramp 1 ℃ min^{-1}). Subsequently, the temperature was increased to 200 ℃ for 2 h (heating ramp 3 ℃ min^{-1}) to consolidate the microstructure. Finally, the

furnace was heated to 600 °C for 1h (heating ramp 3 °C min^{-1}) to eliminate all the remaining organic residues.

2.4 Characterization

The morphology and microstructure of the films were characterized using high resolution scanning and scanning transmission electron microscopies (HR-SEM and HR-STEM, respectively). HR-SEM observations were carried out on a Zeiss Merlin microscope operated at 0.8 keV. Grazing incidence X-ray diffraction (XRD) patterns were recorded on a PANalytical X'pert PRO MRD (Materials Research Diffractometer) using Cu *Kα* radiation (λ = 0.154 nm) at an incidence angle of 1.18°. The patterns were acquired in the 2*θ* angular range varying from 20° to 80° with step time of 0.8 s and step size of 0.03°. The values of crystallite size, microstrains and lattice parameters as a function of Ni doping were extracted from Rietveld refinement of the XRD full-patterns by utilizing the "Materials Analysis using Diffraction" (MAUD) software.[39] HR-STEM analyses were performed on a Tecnai F20 microscope equipped with energy dispersive X-ray spectroscopy (EDX) and selected area electron diffraction (SAED). For STEM-EDX analyses, ultra-thin cross-sections were prepared and placed onto holey carbon Cu TEM grids. The cross-section specimens were obtained by mechanically slicing the mesoporous films, followed by mechanical polishing/thinning and subsequent ion milling. X-ray photoelectron spectroscopy (XPS) analyses (PHI 5500 Multitechnique System) were carried out with a monochromatic X-ray source (K*α* Al line of 1486.6 eV energy and 350 W power) under ultra-high vacuum (UHV), placed perpendicular to the analyzer axis and calibrated using the $3d_{5/2}$ line of Ag with a full width at half maximum (FWHM) of 0.8 eV. During the measurement, the chamber pressure was kept between 5×10^{-9} and 2×10^{-8} Torr. Ar^+ ion etching (1 min) with energy of 3 keV and

ion current density of a few microamperes were applied at a raster circle of 0.8 mm diameter. Peaks were charged corrected to adventitious C 1s set to 284.50 eV. Experimental core-level spectra were fitted using Gaussian curves. A Shirley background subtraction was included in the fitting procedure. Magnetic hysteresis loops were acquired using a vibrating sample magnetometer (VSM) from Micro-Sense (LOT-Quantum Design) at room temperature. To minimize spurious magnetic response from the substrate, all presented loops correspond to the measurements after subtracting the signal of the bare substrate.

3. Results and discussion

3.1 Morphological and structural characterization

The surface morphology of the Ni-doped SnO_2 films was investigated by SEM. Fig. 1 indicates that the films are not fully-dense but, instead, they exhibit a nanoporous morphology. Tiny pores are homogeneously distributed on the whole surface of the samples, irrespective of the [Ni(II)]/[Sn(IV)] molar ratio used in the synthesis. When compared with undoped SnO_2 films (Fig. S1, Supplementary Information), the incorporation of Ni does not seemingly cause any relevant morphological change. Namely, both undoped and Ni-doped films exhibit nanosized worm-like channels throughout the surface and, importantly, they are very flat and crack-free. Low-magnification cross-section SEM images (Fig. S2, Supplementary Information) show that pores span the whole film thickness (which is in the range of 100-150 nm, as indicated in the figure). Table 1 lists the Ni content in the films as determined by XPS analyses. As expected, the amount of Ni increases with the [Ni(II)]/[Sn(IV)] ratio, from 0.0 to 8.6 at.%.

Grazing incidence X-ray diffraction (XRD) patterns reveal that the pore walls are nanocrystalline (Fig. 2). The main peak positions of the undoped and Ni-doped SnO_2 samples correspond to the rutile-type tetragonal structure of SnO_2 (JCPDS card No. 88-0287). Additional diffraction peaks indicated by arrows in Fig. 2 match the positions of SnO (JCPDS card No. 72-1012) and Sn_3O_4 (JCPDS card No. 16-0737). It has been reported that the formation of SnO, SnO_2 and Sn_3O_4 is both oxygen- and temperature-dependent during heat treatment.[40] In our work, however, the temperature was held constant during heat-treatment of all films (600 ºC) and therefore, the occurrence of SnO and Sn_3O_4 cannot be attributed to differences in temperature. The same holds for the atmosphere (i.e., all films were heat-treated in air). Close inspection of the diffractograms reveals that the SnO phase is present in all Ni-doped samples (see the shoulder/peak ca. 51º), although the relative proportion is different, except for the film produced from Ni(II):Sn(IV) 15:85 molar ratio. For this film, the Sn_3O_4 phase is clearly detected. Note that the amount of Ni^{2+} dissolved in the tin oxide lattice is the maximum for this film. Hence, it seems that the occurrence of SnO and Sn_3O_4 phases is linked to the introduction of Ni^{2+} in the material, although the relationship is somewhat complex.

No peaks related to either metallic Ni or NiO are present. This suggests that Ni has entered the SnO_2 lattice. However, the SnO_2 peaks in the diffractograms of the Ni-containing films are not shifted compared to the undoped sample. This can be explained considering the nearly equal ionic radius of Ni^{2+} (0.69 Å) and Sn^{4+} (0.69 Å).[41] The crystallite size of the SnO_2 phase, together with the microstrains and cell parameters, were calculated using the Rietveld method (Table 1). When compared to the undoped sample, the crystallite size decreases in the doped films, although not in a monotonous manner. In turn, the microstrains increase by one order of magnitude, indicating that the incorporation of Ni in the SnO_2 framework induces some strain.

Although the lattice parameters "*a*" and "*c*" do not show pronounced variations upon Ni doping, "*a*" increases while "*c*" decreases with the introduction of Ni (except for the sample synthesized from the 15:85 [Ni(II)]/[Sn(IV)]).

In order to further investigate the overall crystallographic structure and the eventual occurrence of NiO in the films with the highest Ni content, TEM characterization was carried out. The cross-section images and corresponding SAED patterns of the films containing 5.1 and 8.6 at.% Ni are shown in Fig. 3(a) and (b), respectively. Fig. 3 further confirms that the whole films are entirely porous. However, compared with Fig. 3(a), the TEM image of Fig. 3(b) shows some darker areas. The SAED patterns from the marked regions (white circles) are shown in the right panels of Fig. 3(a) and 3(b). The two SAED patterns are similar, although a few spots corresponding to NiO phase are indeed detected for the sample synthesized from [Ni(II)/Sn(IV)] = 20:80 (with 8.6 at.% Ni). It is worth mentioning that whilst pure mesoporous SnO_2 thin films were already synthesized by EISA in the past, to the best of our knowledge there is only one work reporting on the synthesis of mesoporous NiO thin films using this approach.[42] In that work, poly(ethylene-co-butylene)-block-poly(ethylene oxide) (KLE) was employed as structure-directing agent. Here, both materials (SnO_2 and NiO) coexist in the same mesostructured skeleton.

Detailed HR-TEM images of the mesoporous films with 5.1 at.% Ni and 8.6 at.% Ni are shown in Fig. 4. The pore walls consist of tiny crystallites, whose interplanar distances match the SnO_2 tetragonal structure, in agreement with the XRD and SAED results. Sub-10 nm pores are also clearly visible (as indicated in the figure) and the width of the pore walls is in the 5-10 nm range. The size of the crystallites is actually in agreement with the results obtained from Rietveld refinement of the XRD patterns (Table 1). The occurrence of a few

NiO clusters embedded in the Ni-doped SnO_2 nanoporous film is confirmed for the sample with 8.6 at.% Ni (see Fig. 4(b) and (c)) .

To precisely locate the NiO phase within the SnO_2 network, the films with 5.1 and 8.6 at.% Ni (NiO as a secondary phase was clearly detected by SAED in the latter) were selected for EDX mapping characterization. Fig. 5 shows the STEM and corresponding EDX mapping of a selected region for these samples. Remarkably, for the mesoporous film with the highest Ni amount, several bright areas (notice that the contrast is the opposite in TEM images) were visible in the film cross-section. EDX mappings of a zoomed detail of the cross-sections were conducted to determine the distribution of Sn, Ni and O elements (top panel of Fig. 4(a) and 4(b)). In both cases, O and Sn elements are distributed rather homogeneously across the whole area. Ni is also evenly distributed in the film with 5.1 at.% Ni but not in the film with 8.6 at.% Ni. For this sample, Ni preferably accumulates in the brighter area. This result is in agreement with previous TEM and SAED analyses and suggests that, although no peaks from NiO can be detected by XRD (because their amounts are below the detection limit of the XRD technique), a few aggregates enriched in Ni of around 20 nm are indeed formed for sufficiently large Ni contents. Note that these aggregates do not apparently show a mesoporous structure (see Figure 3b and 5b). The aggregates are denser, which is very clear from the cross-section STEM images. Hence, the formation of these aggregates partially disrupts the mesostructure of SnO_2. This is the reason why their size is larger than the pore wall thickness of SnO_2.

3.2 XPS characterization

To shed light on the valence state of Ni and the occurrence of oxygen vacancies in the Ni-doped mesoporous films, XPS characterization was carried out. Fig. 6(a) shows the survey

spectra of all samples including undoped SnO_2, taken as a reference sample. The corresponding core-level Sn 3d is displayed in Fig. 6(b). The peaks belonging to Sn $3d_{5/2}$ and $3d_{3/2}$ located at ~ 486.1 eV and ~ 495.5 eV are assigned to SnO_2.[43,44] A slight shift toward higher binding energies is noted for the films with the highest Ni contents (5.1 and 8.6 at.%).

As shown in Fig. 6(c) and 6(d), the O 1s spectrum for the samples containing 5.1 and 8.6 at.% Ni can be deconvoluted into three main bands centered at 529.58 eV, 530.25 eV and 531.66 eV. The peaks located at 529.58 eV and 530.25 eV are attributed to O^{2-} anions in the SnO_2 (and NiO) lattice,[45–47] whereas the peak at 531.66 eV is associated with O ion in oxygen deficient regions or oxygen vacancies in the lattice.[48] This peak might be also attributed to hydroxyl groups. Actually, assignation to both adsorbed oxygen (OH^- groups) on the surface or oxygen vacancies is stated by some authors.[49,50] However, when compared with undoped SnO_2 film, there is a clear shift of the O 1s peak toward higher binding energy, suggesting that the Ni incorporation into SnO_2 structure gradually generates oxygen vacancies up to 5.1 at.% Ni (see Fig. S3(a) in the Supplementary Information).

The corresponding Ni 2p core-level XPS spectra for the samples containing 5.1 and 8.6 at.% Ni are shown in Fig. 6(e) and 6(f), respectively (see spectra for all samples in Fig. S3(b) of the Supplementary Information). In this case, the profiles show some remarkable differences. In particular, the peak contribution with a binding energy around 855.5 eV (Ni $2p_{3/2}$) assigned to Ni^{2+} in NiO notoriously increases in Fig. 6(f) compared to Fig. 6(e) (see also Table 2). This is in agreement with both the observed increase in the total amount of Ni incorporated into the film and the formation of relatively large NiO particles. Besides, the Ni $2p_{3/2}$ peak located at ~530.0 eV could be attributed to monovalent Ni species.[51,52] Therefore, Ni possesses a mixed valence state of 1+/2+.

3.3 Magnetic properties of Ni-doped SnO_2 films

The magnetic properties of the samples with varying Ni concentration were first studied by acquiring hysteresis loops at room temperature and subtracting the signal from the bare substrates. As shown in Fig. 7, the undoped SnO_2 film exhibits a diamagnetic behavior (negative magnetization *vs.* field slope), in agreement with previous studies on this type of oxide semiconductors.[53] Conversely, a clear (positive) paramagnetic slope dominates the magnetic behavior of the samples with the highest Ni amounts (5.1 and 8.6 at.% Ni). This positive slope can be attributed to the presence of NiO clusters, as evidenced by EDX and SAED analyses. Note that although bulk NiO is antiferromagnetic with a Néel temperature, T_N, of around 520 K, typically T_N is considerably reduced in nanoparticles compared to the bulk. Superimposed to this positive linear background, a small ferromagnetic signal is observed. The origin of ferromagnetism in oxide diluted semiconductors is, in fact, a topic of extensive research by many research groups. Contradictory results are easily found in the literature, depending on the material under investigation (bulk, thin films, nanoparticles) and the synthetic procedures, even when the same composition is maintained. In our case, the small ferromagnetic response cannot be attributed to the presence of metallic Ni clusters, since no evidence of their existence were obtained by TEM, XRD or XPS. Conversely, the small ferromagnetic response could be ascribed to the combined effect from the doping TM and the presence of oxygen vacancies, in agreement with previous works on undoped SnO_2 films,[53] TM-doped dense oxide semiconductor films[54,55] and TM-doped InO_2[35,36] and SnO_2 mesoporous powders.[37] Actually, a mechanism based on ferromagnetic exchange interactions mediated by shallow donor electrons trapped in oxygen vacancies was proposed to account for room-temperature ferromagnetism in dilute ferromagnetic oxides and nitrides.[55] Ab-initio

energy-band calculations showed later that the donor impurities mainly consisted of hybridized 3d–4s TM-cation electronic states.[55] This model was later confirmed by a number of works, both theoretical and experimental ones.[57-60] Nonetheless, because of size and surface effects, full understanding of the magnetic properties of the investigated material is not easy. Uncompensated spins from antiferromagnetic NiO aggregates could contribute to some extent to the observed hysteresis behavior[61] although, as aforementioned, NiO is probably paramagnetic at room temperature. The films with intermediate Ni contents show a virtually zero and small positive magnetization versus applied field slope, respectively. This is due to the interplay between the diamagnetic response from SnO_2 and the paramagnetic background stemming from the secondary NiO phase. Finally, hysteresis loops corresponding to Ni-doped SnO_2 mesoporous films (with 5.1 and 8.6 at.% Ni) were also measured at 100 K, 200 K and 296 K. The results are shown in Figure 8. There is a clear increase in the high-field slope in both samples as temperature is decreased. It is well known that in paramagnetic materials, the susceptibility decreases with temperature, following the Curie-Weiss law. That can explain the change in the slope of the hysteresis loops. It could also be that the NiO clusters become truly antiferromagnetic at low temperatures and that could also give rise to an increase of the high-field magnetization, compared to the high-temperature paramagnetic state. Remarkably, the coercivity of the ferromagnetic-like contribution does not show a pronounced temperature dependence. It remains around 40-60 Oe at the three measured temperatures. Hence, the magnetic response contains a soft-ferromagnetic contribution at all temperatures.

4. Conclusions

Undoped and Ni-doped SnO_2 mesoporous films, containing different amounts of Ni, were successfully synthesized by evaporation induced self-assembly using P-123 as structure directing agent. Truly 3D nanoporous structures, with pore size in the range 5-10 nm, were observed in all mesoporous films. A deep structural characterization reveals that the mesoporous films mainly consist of the rutile-type tetragonal structure of SnO_2, although NiO clusters are formed in samples with large Ni contents (e.g., 8.6 at.% Ni). The mesoporous films also contain large amounts of oxygen vacancies, as revealed by XPS analyses. From a magnetic viewpoint, the incorporation of Ni drastically changes the magnetic response, from a purely diamagnetic one (undoped mesoporous SnO_2) to a mainly paramagnetic one with a small ferromagnetic contribution (in the samples containing Ni). This work opens up new prospects for the use of mesoporous oxide semiconductor thin films with magnetic characteristics in new types of memory and spintronics devices, which could eventually be controlled by various means (e.g., electrolyte gating).

Acknowledgements

This work has been partially funded by the 2014-SGR-1015 project from the Generalitat de Catalunya, the MAT2014-57960-C3-1-R (co-financed by the Fondo Europeo de Desarrollo Regional, FEDER) from the Spanish Ministerio de Economía y Competitividad (MINECO) and the SPIN-PORICS 2014-Consolidator Grant from the European Research Council (Grant Agreement 648454). J. F. acknowledges the China Scholarship Council (CSC) for his PhD grant (201406220145). A.C.-G. acknowledges the financial support from the French Agence

Nationale pour la Recherche (ANR), projet Q-NOSS ANR ANR-16-CE09-0006-01. E. P. is grateful to MINECO for the “Ramon y Cajal” contract (RYC-2012-10839).

References

1. S. Lany, Semiconducting transition metal oxides, *J. Phys.: Condens. Matter*, 2015, **27**, 283203.

2. X. Yu, T. J. Marks, A. Facchetti, Metal oxides for optoelectronic applications, *Nature Mater.*, 2016, **15**, 383–396.

3. J. Huang, Q. Wan, Gas sensors based on semiconducting metal oxide one-dimensional nanostructures, *Sensors*, 2009, **9**, 9903–9924.

4. J. Meyer, S. Hamwi, M. Kröger, W. Kowalsky, T. Riedl, A. Kahn, Transition metal oxides for organic electronics: energetics, device physics and applications, *Adv. Mater.*, 2012, **24**, 5408–5427.

5. C. Yuan, H. B. Wu, Y. Xie, X. W. Lou, Mixed transition-metal oxides: design, synthesis, and energy-related applications, *Angew. Chem. Int. Ed.* 2014, **53**, 1488–1504.

6. J. Hong Pan, X. S. Zhao, W. I. Lee, Block copolymer-templated synthesis of highly organized mesoporous TiO_2-based films and their photoelectrochemical applications, *Chem. Eng. J.*, 2011, **170**, 363–380.

7. T. Dietl, A ten-year perspective on dilute magnetic semiconductors and oxides, *Nature Mater.*, 2010, **9**, 965–974.

8. R. S. Chen, W. C. Wang, C. H. Chan, M. L. Lu, Y. F. Chen, H. C. Lin, K. H. Chen, L. C. Chen, Photoconduction efficiencies of metal oxide semiconductor nanowires: the material's inherent properties, *Appl. Phys. Lett.*, 2013, **103**, 223107.

9. Y. Tian, S. R. Bakaul, T. Wu, Oxide nanowires for spintronics: materials and devices, *Nanoscale*, 2012, **4**, 1529–1540.

10. Y. Ren, Z. Ma, P. G. Bruce, Ordered mesoporous metal oxides: synthesis and applications, *Chem. Soc. Rev.*, 2012, **41**, 4909–4927.

11. T. Wagner, S. Haffer, C. Weinberger, D. Klaus, M. Tiemann, Mesoporous materials as gas sensors, *Chem. Soc. Rev*., 2013, **42**, 4036–4053.

12. D. Gu, F. Schüth, Synthesis of non-siliceous mesoporous oxides, *Chem. Soc. Rev.*, 2014, **43**, 313–344.

13. V. Malgras, H. Ataee-Esfahani, H. Wang, B. Jiang, C. Li, K. C.-W. Wu, J. H. Kim, Y. Yamauchi, Nanoarchitectures for mesoporous metals, *Adv. Mater*., 2016, **28**, 993–1010.

14. A. Walcarius, Mesoporous materials and electrochemistry, *Chem. Soc. Rev.*, 2013, **42**, 4098–4140.

15. N. Pal, A. Bhaumik, Soft templating strategies for the synthesis of mesoporous materials: Inorganic, organic–inorganic hybrid and purely organic solids, *Adv. Colloid Interface Sci.*, 2013, **189–190**, 21–41.

16. A.-H. Lu, D. Zhao, Y. Wan, *Nanocasting: A versatile strategy for creating nanostructured porous materials*, Royal Society of Chemistry: Cambridge, U.K., 2009.

17. G. J. d. A. A. Soler-Illia, E. L. Crepaldi, D. Grosso, C. Sanchez, Block copolymer-templated mesoporous oxides, *Curr. Opin. Colloid Interface Sci*., 2003, **8**, 109–126.

18. S. Wang, P. Tangvijitsakul, Z. Qiang, S. M. Bhaway, K. Lin, K. A. Cavicchi, M. D. Soucek, B. D. Vogt, Role of amphiphilic block copolymer composition on pore characteristics of micelle-templated mesoporous cobalt oxide films, *Langmuir*, 2016, **32**, 4077-4085.

19. L. Jia, W. Cai, Micro/nanostructured ordered porous films and their structurally induced control of the gas sensing performances, *Adv. Funct. Mater*., 2010, **20**, 3765–3773.

20. Y. F. Lu, R. Ganguli, C. A. Drewien, M. T. Anderson, C. J. Brinker, W. L. Gong, Y. X. Guo, H. Soyez, B. Dunn, M. H. Huang, J. I. Zink, Continuous formation of supported cubic and hexagonal mesoporous films by sol gel dip-coating, *Nature*, 1997, **389**, 364–368.

21. C. J. Brinker, Y. Lu, A. Sellinger, H. Fan, Evaporation-induced self-assembly: nanostructures made easy, *Adv. Mater.*, 1999, **11**, 579–585.

22. T. Brezesinski, M. Groenewolt, A. Gibaud, N. Pinna, M. Antonietti, B. M. Smarsly, Evaporation-induced self-assembly (EISA) at its limit: ultrathin, crystalline patterns by templating of micellar monolayers, *Adv. Mater*., 2006, **18**, 2260–2263.

23. L. Li, H. Lin, F. Qu, Synthesis of mesoporous SnO_2 nanomaterials with selective gas-sensing properties, *J. Sol-Gel Sci. Technol*., 2013, **67**, 545–555.

24. T. Wagner, C.-D. Kohl, M. Fröba, M. Tiemann, Gas sensing properties of ordered mesoporous SnO_2, *Sensors*, 2006, **6**, 318–323.

25. T. Brezesinski, A. Fischer, K.-i. Iimura, C. Sanchez, D. Grosso, M. Antonietti, B. M. Smarsly, Generation of self-assembled 3D mesostructured SnO_2 thin films with highly crystalline frameworks, *Adv. Funct. Mater*., 2006, **16**, 1433–1440.

26. S. Shao, M. Dimitrov, N. Guan, R. Köhn, Crystalline nanoporous metal oxide thin films by post-synthetic hydrothermal transformation: SnO_2 and TiO_2, *Nanoscale*, 2010, **2**, 2054–2057.

27. J. H. Pan, D. D. Sun, W. I. Lee, Preparation of periodically organized mesoporous bicomponent TiO_2 and SnO_2-based thin films by controlling the hydrolytic kinetics of inorganic precursors during EISA process, *Mater. Lett.*, 2011, **65**, 2836–2840.

28. D. I. Fried, A. Ivanova, V. Müller, J. Rathousky, B. M. Smarsly, D. Fattakhova-Rohlfing, A facile synthesis of mesoporous crystalline tin oxide films involving a base-triggered formation of sol–gel building blocks, *Nanoscale*, 2011, **3**, 1234–1239.

29. J. H. Pan, S. Y. Chai, C. Lee, S.-E. Park, W. I. Lee, Controlled formation of highly crystallized cubic and hexagonal mesoporous SnO_2 thin films, *J. Phys. Chem. C*, 2007, **111**, 5582–5587.

30. J. Fan, G. Zhao, H. Zhao, S. Chai, T. Cao, Fabrication and application of mesoporous Sb-doped SnO_2 electrode with high specific surface in electrochemical degradation of ketoprofen, *Electrochim. Acta*, 2013, **94**, 21-29.

31. V. Müller, M. Rasp, J. Rathouský, B. Schütz, M. Niederberger, D. Fattakhova-Rohlfing, Transparent conducting films of antimony-doped tin oxide with uniform mesostructure assembled from preformed nanocrystals, *Small*, 2010, **6**, 633–637.

32. Y. Wang, T. Brezesinski, M. Antonietti, B. Smarsly, Ordered mesoporous Sb-, Nb-, and Ta-doped SnO_2 thin films with adjustable doping levels and high electrical conductivity, *ACS Nano*, 2009, **3**, 1373–1378.

33. C. Reitz, C. Suchomski, J. Haetge, T. Leichtweiss, Z. Jaglicic, I. Djerdj, T. Brezesinski, Soft-templating synthesis of mesoporous magnetic $CuFe_2O_4$ thin films with ordered 3D honeycomb structure and partially inverted nanocrystalline spinel domains, *Chem. Commun*., 2012, **48**, 4471–4473.

34. T. E. Quickel, L. T. Schelhas, R. A. Farrell, N. Petkov, V. H. Le, S. H. Tolbert, Mesoporous bismuth ferrite with amplified magnetoelectric coupling and electric field-induced ferromagnetism, Nature Comm. 2015, **6**, 6562.

35. E. Pellicer, M. Cabo, E. Rossinyol, P. Solsona, S. Suriñach, M. D. Baró, J. Sort, Nanocasting of mesoporous In-TM (TM = Co, Fe, Mn) oxides: towards 3D diluted-oxide magnetic semiconductor architectures, *Adv. Funct. Mater.*, 2013, **23**, 900–911.

36. E. Pellicer, E. Menéndez, J. Fornell, J. Nogués, A. Vantomme, K. Temst, J. Sort, Mesoporous oxide-diluted magnetic semiconductors prepared by Co implantation in nanocast 3D-ordered In_2O_{3-y} materials, *J. Phys. Chem. C*, 2013, **117**, 17084–17091.

37. J. Fan, J. Zhang, P. Solsona, S. Suriñach, M. D. Baró, J. Sort, E. Pellicer, Nanocasting synthesis of mesoporous SnO_2 with a tunable ferromagnetic response through Ni loading, *RSC Adv.*, 2016, **6**, 104799–104807.

38. C. Reitz, D. Wang, D. Stoeckel, A. Beck, T. Leichtweiss, H. Hahn, T. Brezesinski, Applying capacitive energy storage for in situ manipulation of magnetization in ordered mesoporous perovskite-type LSMO thin films, *ACS Appl. Mater. Interfaces*, in press, 10.1021/acsami.7b01978.

39. L. Lutterotti, S. Matthies, H.-R. Wenk, MAUD: a friendly Java program for material analysis using diffraction, *IUCr: Newsl. CPD*, 1999, **21**, 14–15.

40. P. H. Suman, A. A. Felix, H. L. Tuller, J. A. Varela, M. O. Orlandi, Comparative gas sensor response of SnO_2, SnO and Sn_3O_4 nanobelts to NO_2 and potential interferents, Sens. Act. B. Chem., 2015, 208, 122-127.

41. K. Barbalace. *Periodic Table of Elements - Sorted by Ionic Radius*. EnvironmentalChemistry.com, (1995-2017). Accessed on-line: 1/3/2017, http://EnvironmentalChemistry.com/yogi/periodic/ionicradius.html.

42. M. Bernicke, B. Eckhardt, A. Lippitz, E. Ortel, D. Bernsmeier, R. Schmack, R. Kraehnert, Synthesis and OER activity of NiO coatings with micelle–templated mesopore structure, *ChemistrySelect* 2016, **3**, 482–489.

43. R. Shiratsuchi, K. Hongo, G. Nogami, Reduction of CO_2 on Fluorine - Doped SnO_2 Thin-Film Electrodes, *J. Electrochem. Soc.*, 1992, **139**, 2544–2549.

44. M. Batzill, J. Kim, D. E. Beck, B. E. Koel, Epitaxial growth of tin oxide on Pt(111): Structure and properties of wetting layers and SnO_2 crystallites, *Phys. Rev. B*, 2004, **69**, 165403-1-11.

45. D. L. Legrand, H. W. Nesbitt, G. M. Bancroft, X-ray photoelectron spectroscopic study of a pristine millerite (NiS) surface and the effect of air and water oxidation, *Am. Mineral.*, 1998, **83**, 1256–1265.

46. M. Kwoka, L. Ottaviano, M. Passacantando, S. Santucci, G. Czempik, J. Szuber, XPS study of the surface chemistry of L-CVD SnO_2 thin films after oxidation, *Thin Solid Films*, 2005, **490**, 36–42.

47. A. Thogersen, M. Rein, E. Monakhov, J. Mayandi, S. Diplas, Elemental distribution and oxygen deficiency of magnetron sputtered indium tin oxide films, *J. Appl. Phys*., 2011, **109**, 113532-1-8.

48. R. Noonuruk, W. Mekprasart, N. Vittayakorn, J. Sritharathikhun, W. Pecharapa, Physical, electrical and optical properties of F/Sb codoped SnO_2 synthesized via sonochemical process, *Ferroelectrics*, 2016, **490**, 136–148.

49. S. K. Alla, R. K. Mandal, N. K. Prasad, Optical and magnetic properties of Mg^{2+} doped CeO_2 nanoparticles, *RSC Adv*. 2016, **6**, 103491.

50. N. Paunovic, Z. Dohcevic-Mitrovic, R. Scurtu, S. Askrabic, M. Prekajski, B. Matovic, Z. V. Popovic, Suppression of inherent ferromagnetism in Pr-doped CeO_2 nanocrystals, *Nanoscale* 2012, **4**, 5469–5476.

51. G. D. Park, J. S. Cho, Y. C. Kang, Sodium-ion storage properties of nickel sulfide hollow nanospheres/reduced graphene oxide composite powders prepared by a spray drying process and the nanoscale Kirkendall effect, *Nanoscale*, 2015, **7**, 16781–16788.

52. S. N. Oliaee, C. Zhang, S. Y. Hwang, H. M. Cheung, Z. Peng, Synthesis and property of a Helwingia-structured nickel nitride/ nickel hydroxide nanocatalyst in hydrazine decomposition, *RSC Adv*., 2016, **6**, 38494–38498.

53. G. S. Chang, J. Forrest, E. Z. Kurmaev, A. N. Morozovska, M. D. Glinchuk, J. A. McLeod, A. Moewes, T. P. Surkova, N. H. Hong, Oxygen-vacancy-induced ferromagnetism in undoped SnO_2 thin films, *Phys. Rev. B*, 2012, **85**, 165319-1-5.

54. Y. Matsumoto, M. Murakami, T. Shono, T. Hasegawa, T. Fukumura, M. Kawasaki, P. Ahmet, T. Chikyow, S.-y. Koshihara, H. Koinuma, Room-temperature ferromagnetism in transparent transition metal-doped titanium dioxide, *Science*, 2001, **291**, 854–856.

55. J. M. D. Coey, M. Venkatesan, C. B. Fitzgerald, Donor impurity band exchange in dilute ferromagnetic oxides, *Nat. Mater.* 2005, **4**, 173–179.

56. S.-j. Hu, S.-s. Yan, X.-l. Lin, X.-x. Yao, Y.-x. Chen, G.-l. Liu, L.-m. Mei, Electronic structure of Fe-doped In_2O_3 magnetic semiconductor with oxygen vacancies: Evidence for F-center mediated exchange interaction, *Appl. Phys. Lett.*, 2007, **91**, 262514-1-3.

57. A. M. H. R. Hakimi, F. Schoofs, R. Bali, N. A. Stelmashenko, M. G. Blamire, S. Langridge, S. A. Cavill, G. van der Laan , S. S. Dhesi, Origin of magnetism in cobalt-doped indium tin oxide thin films, *Phys. Rev. B*, 2010, **82**, 144429-1-7.

58. A. M. H. R. Hakimi, M. G. Blamire, S. M. Heald, M. S. Alshammari, M. S. Alqahtani, D. S. Score, H. J. Blythe, A. M. Fox, G. A. Gehring, Donor-band ferromagnetism in cobalt-doped indium oxide, *Phys. Rev. B*, 2011, **84**, 085201-1-8.

59. N. H. Hong, J. Sakai, N. Poirot, V. Brizé, Room-temperature ferromagnetism observed in undoped semiconducting and insulating oxide thin films, *Phys. Rev. B*, 2006, **73**, 132404-1-4.

60. D. Bérardan, E. Guilmeau, Magnetic properties of bulk Fe-doped indium oxide, *J. Phys.: Condens. Matter*, 2007, **19**, 236224.

61. R. H. Kodama, S. A. Makhlouf, A. E. Berkowitz, Finite size effects in antiferromagnetic NiO nanoparticles, *Phys. Rev. Lett.*, 1997, **79**, 1393-1396.

[Ni(II)]/[Sn(IV)]	Actual Ni content (from XPS) (at.%)	Crystallite size of SnO_2 phase (nm) (± 0.8)	Microstrains of SnO_2 phase ($\pm 3 \cdot 10^{-5}$)	*a* (Å) of SnO_2 phase ($\pm 2 \cdot 10^{-3}$)	*c* (Å) of SnO_2 phase ($\pm 2 \cdot 10^{-3}$)
0:100	0.0	9.7	$1.1 \cdot 10^{-4}$	4.726	3.182
5:95	1.9	6.2	$2.6 \cdot 10^{-3}$	4.729	3.187
10:90	4.8	6.4	$5.1 \cdot 10^{-3}$	4.731	3.184
15:85	5.1	7.4	$5.3 \cdot 10^{-3}$	4.721	3.178
20:80	8.6	7.5	$4.5 \cdot 10^{-3}$	4.736	3.183

Table 1. Crystallite size, microstrains and cell parameters of the SnO_2 phase in the undoped and Ni-doped SnO_2 films as a function of the [Ni(II)]/[Sn(IV)] molar ration used the synthesis.

Actual Ni content (from XPS) (at.%)	Valence state	Binding energy (eV) $2p_{3/2}$	Binding energy (eV) $2p_{1/2}$
5.1	Ni^{1+}	852.9	870.1
	Ni^{2+}	855.3	872.4
8.6	Ni^{1+}	852.6	869.8
	Ni^{2+}	855.5	872.9

Table 2. Binding energy of the spectral fitting for Ni $2p_{3/2}$ and Ni $2p_{1/2}$.

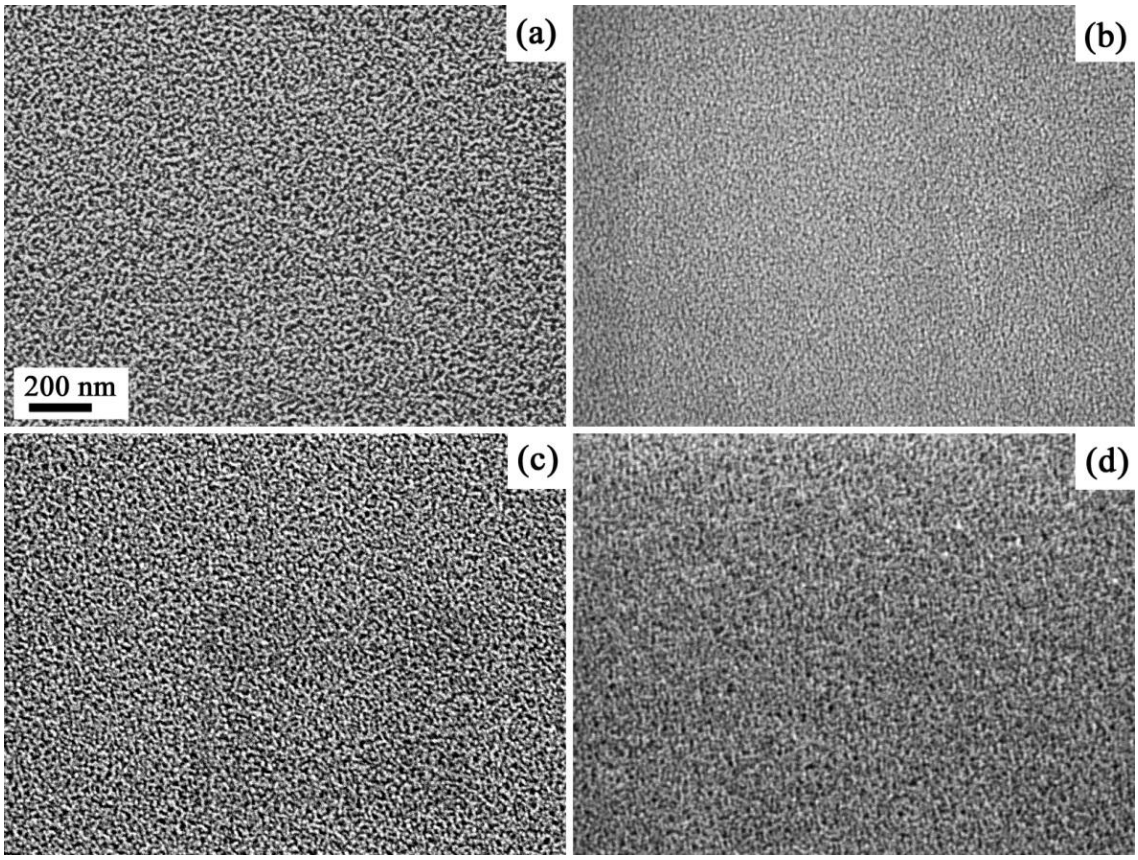

Fig. 1: On-top SEM images of Ni-doped SnO_2 mesoporous films synthesized from variable [Ni(II)/Sn(IV)] molar ratios: (a) 5:95, (b) 10:90, (c) 15:85 and (d) 20:80. The scale bar is the same for all images.

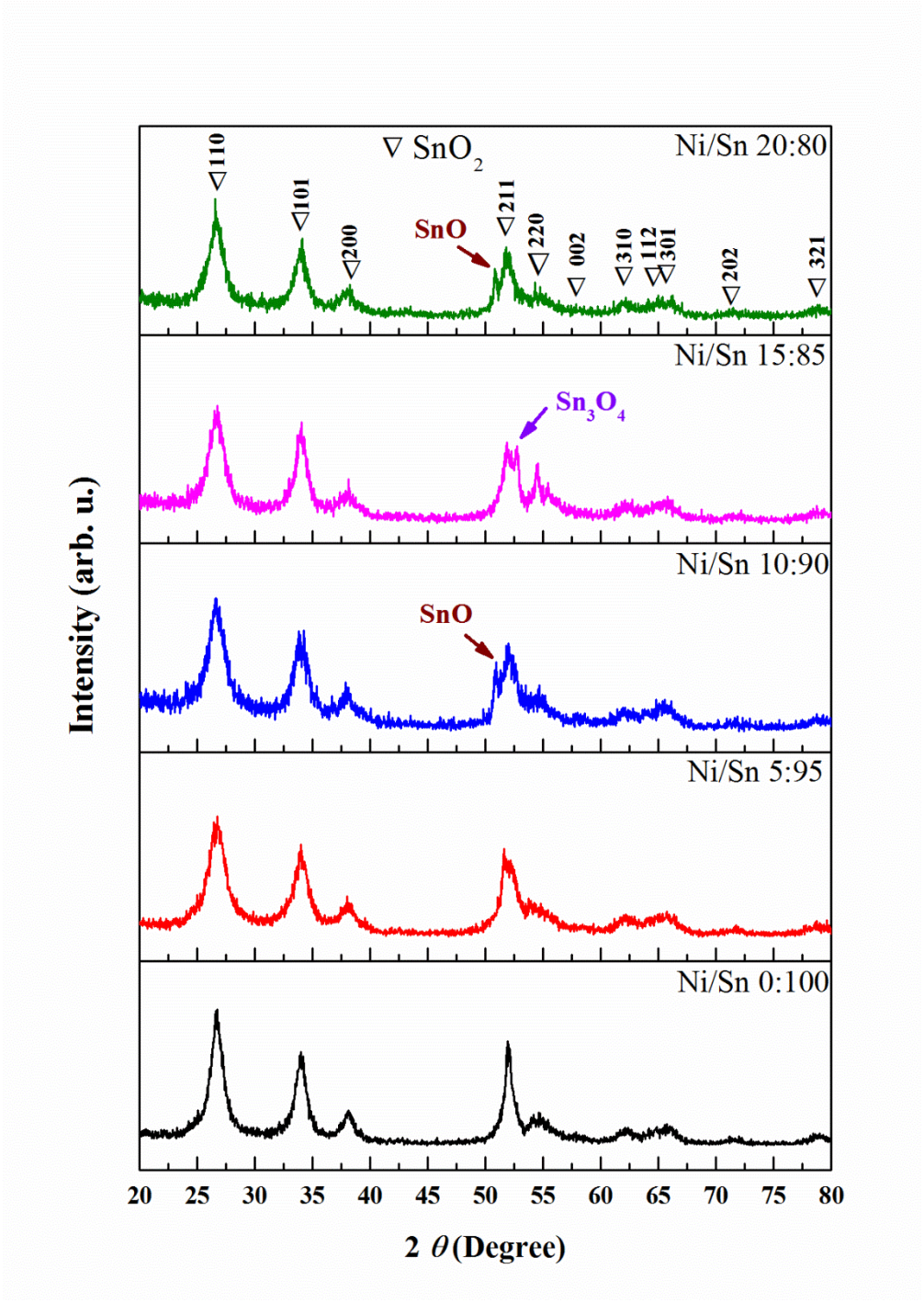

Fig. 2: Grazing incidence XRD patterns of mesoporous undoped and Ni-doped SnO_2 films synthesized from varying [Ni(II)]/[Sn(IV)] molar ratios.

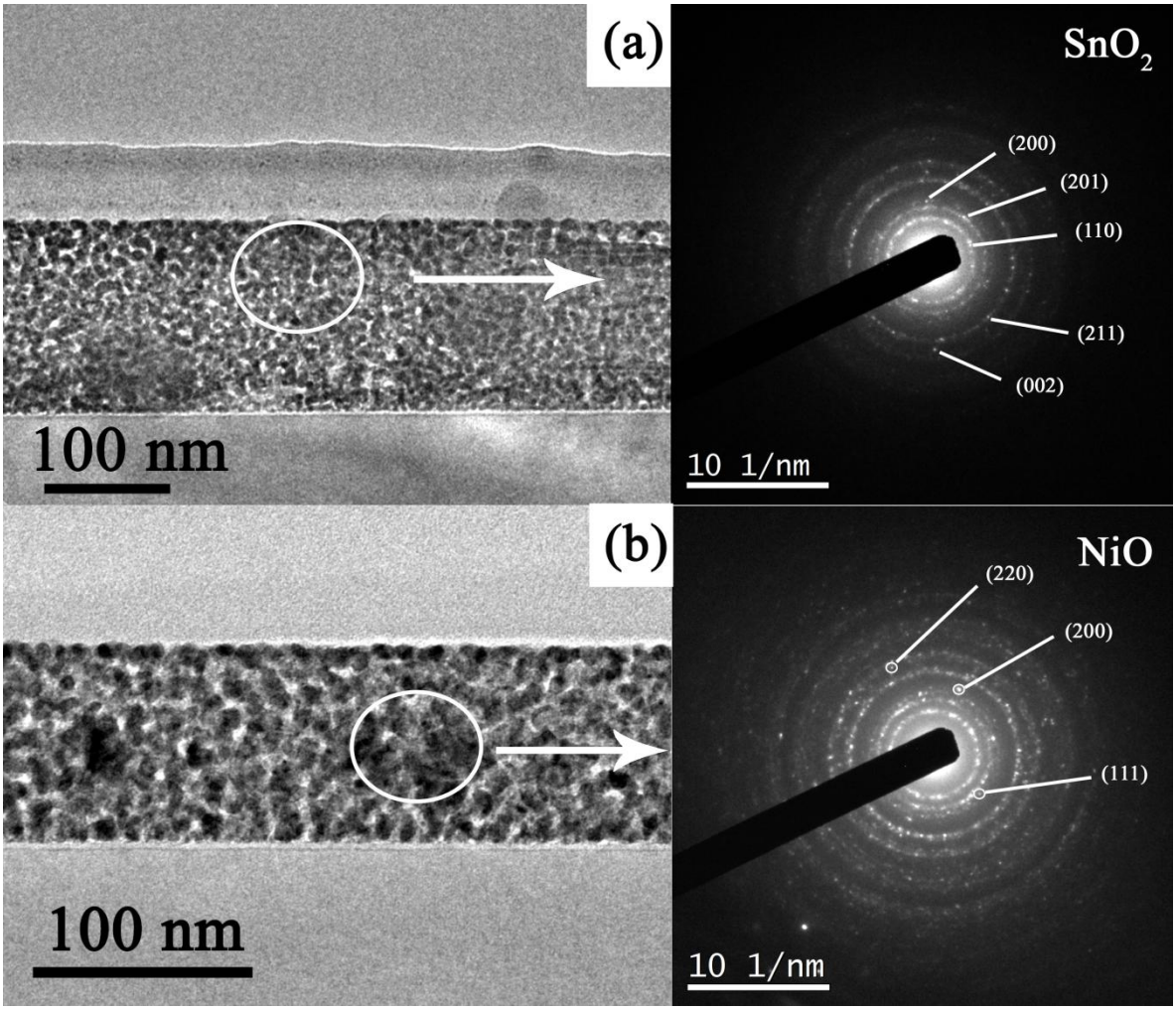

Fig. 3: TEM images (left) and SAED patterns (right) of the cross-sections of the mesoporous Ni-doped SnO_2 thin films with (a) 5.1 at.% Ni, and (b) 8.6 at.% Ni. The indicated planes in (a) correspond to the SnO_2 phase whereas only those corresponding to the NiO phase have been indicated in (b) for the sake of clarity.

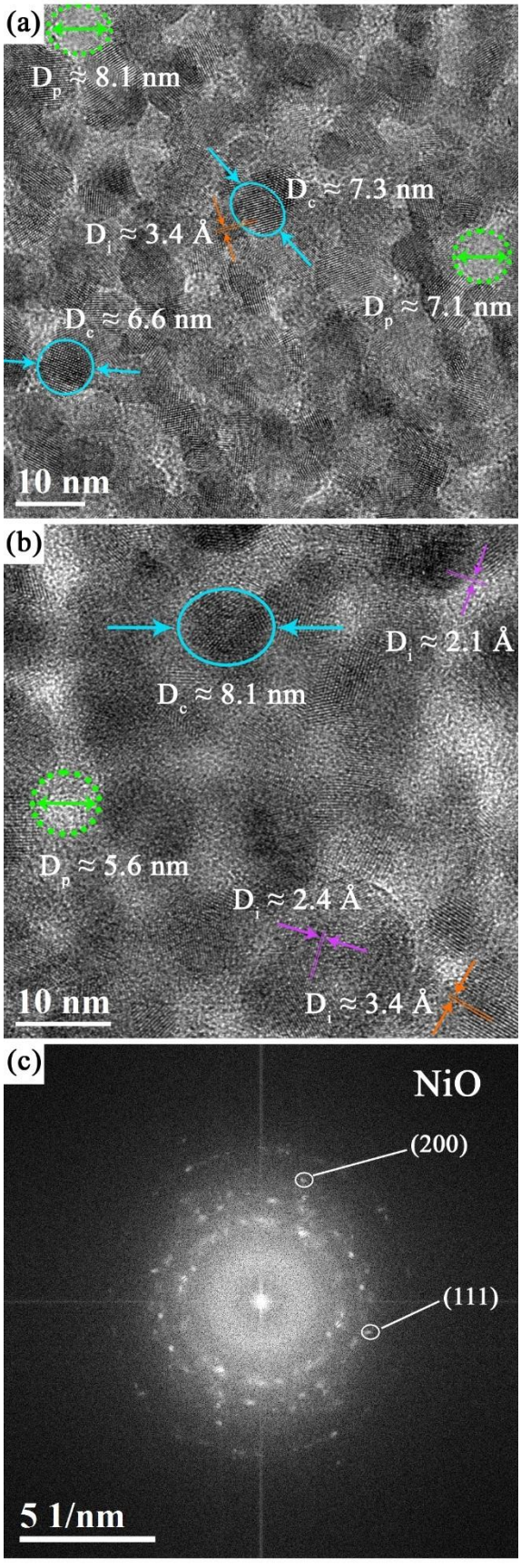
(a)
D_p ≈ 8.1 nm
D_c ≈ 7.3 nm
D_i ≈ 3.4 Å
D_p ≈ 7.1 nm
D_c ≈ 6.6 nm
10 nm
(b)
D_i ≈ 2.1 Å
D_c ≈ 8.1 nm
D_p ≈ 5.6 nm
D_i ≈ 2.4 Å
D_i ≈ 3.4 Å
10 nm
(c)
NiO
(200)
(111)
5 1/nm

Fig. 4: HR-TEM image corresponding to the mesoporous film with [Ni(II)/Sn(IV)] equal to (a) 15:85 (with 5.1 at.% Ni) and (b) 20:80 (with 8.6 at.% Ni). D_c denotes the diameter of the crystallites in the pore wall (a couple of them are indicated with blue cyan circles) and D_p indicates the diameter of the pores (two of them indicated with green circles). Orange-colored D_i represents the interplanar distance in one of the crystallites composing the pore walls (D_i = 3.4 Å matches the (110) planes of the tetragonal SnO_2 phase). Purple-colored D_i corresponds to an interplanar distance of NiO clusters in sample (b). (c) Fast Fourier Transform (FFT) image of the HRTEM image shown in (b). Some spots corresponding to NiO phase are indicated.

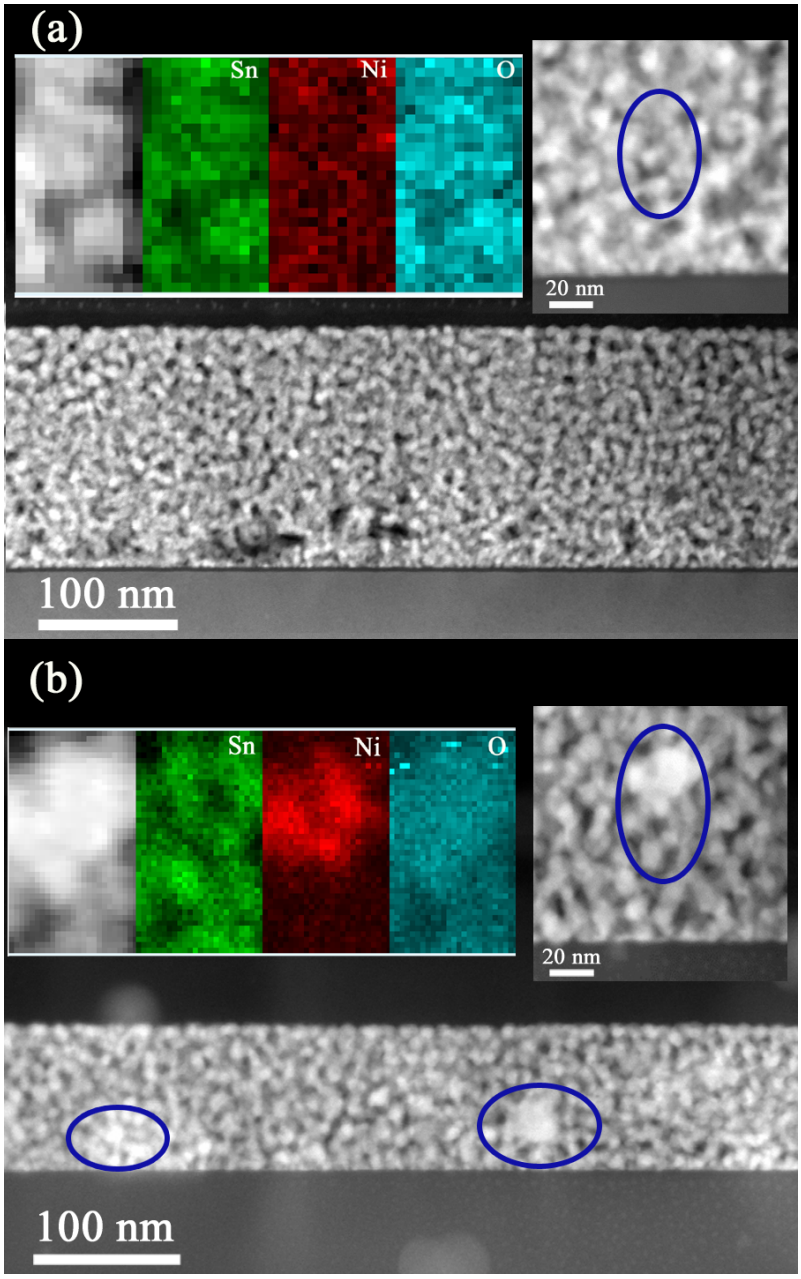

Fig. 5: Cross-section STEM images (bottom) and elemental EDX mappings (top) of the samples with 5.1 and 8.6 at% Ni. The distribution of Sn, Ni and O elements correspond to the encircled area shown in the STEM image detail of the upper right panel.

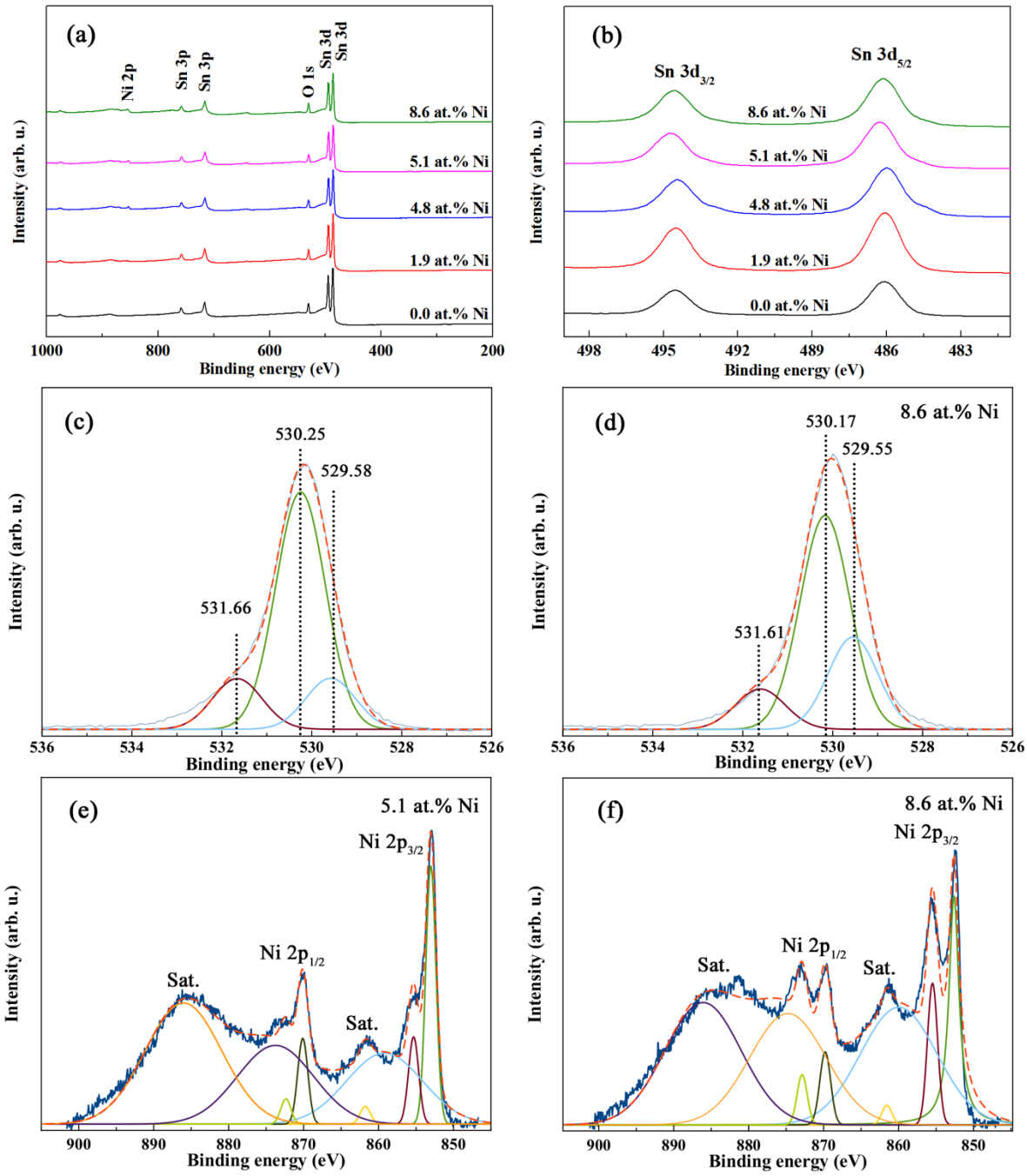

Fig. 6: (a) General XPS survey spectra of undoped and Ni-doped SnO_2 mesoporous films, (b) high resolution XPS spectra of Sn 3d. The corresponding deconvolution of O 1s [(c) and (d)] and Ni 2p [(e) and (f)] are shown for the films with 5.1 and 8.6 at.% Ni, respectively. "Sat." denotes satellite peaks.

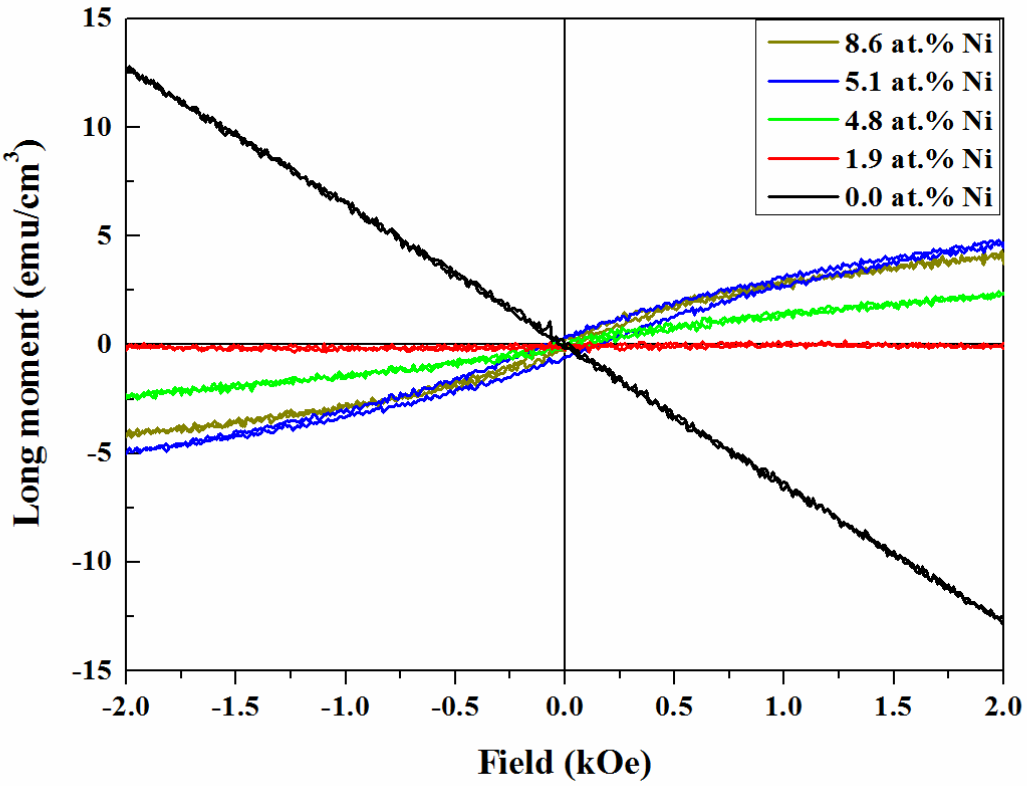

Fig. 7: Magnetic hysteresis loops of undoped and Ni-doped SnO_2 mesoporous films at room temperature. Long moment refers to in-plane magnetization.

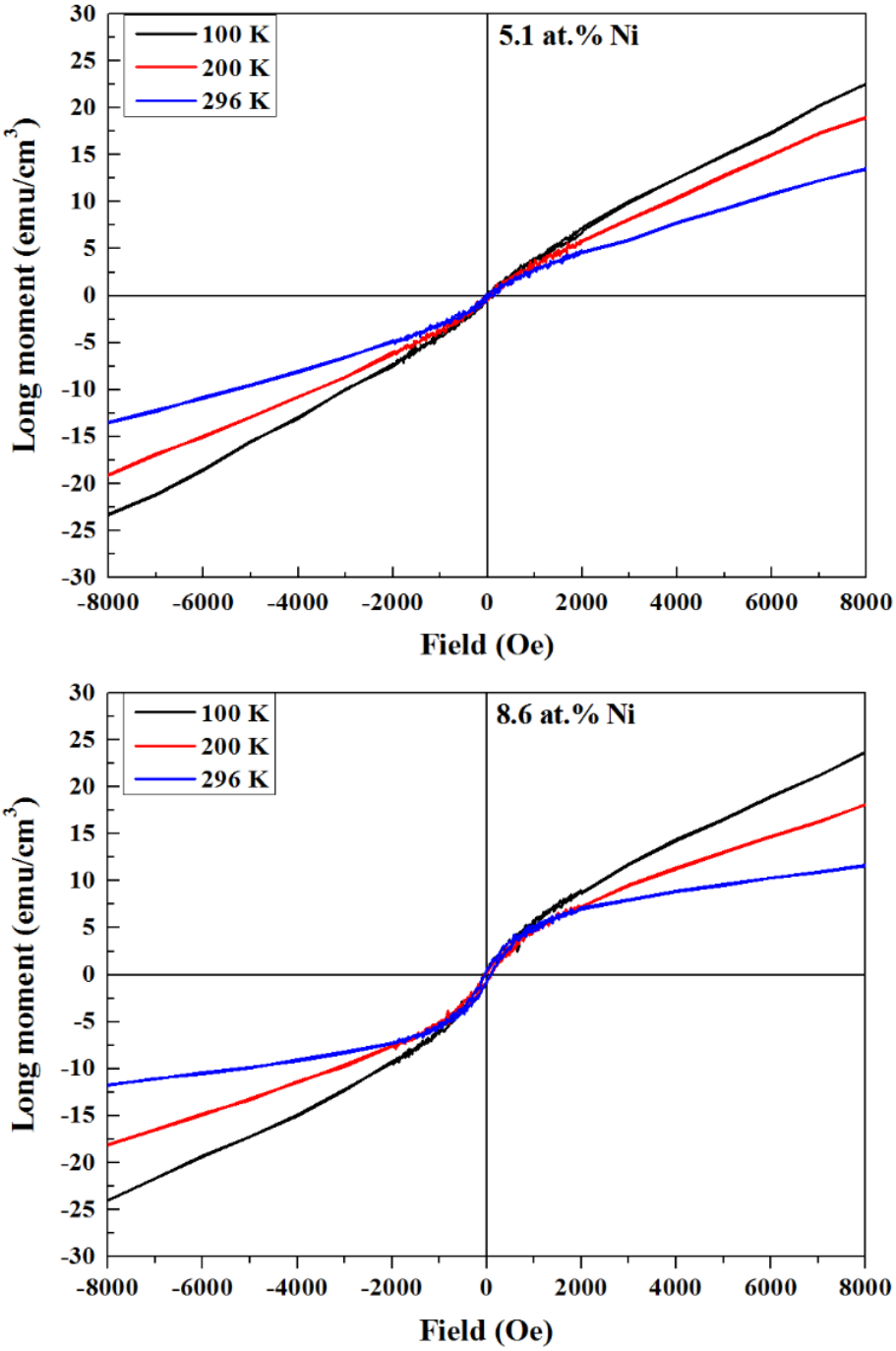

Fig. 8: Comparison of the hysteresis loops corresponding to Ni-doped SnO_2 mesoporous films (with 5.1 and 8.6 at.% Ni) measured at 100 K, 200 K and 296 K. Long moment refers to in-plane magnetization.

Supplementary Information

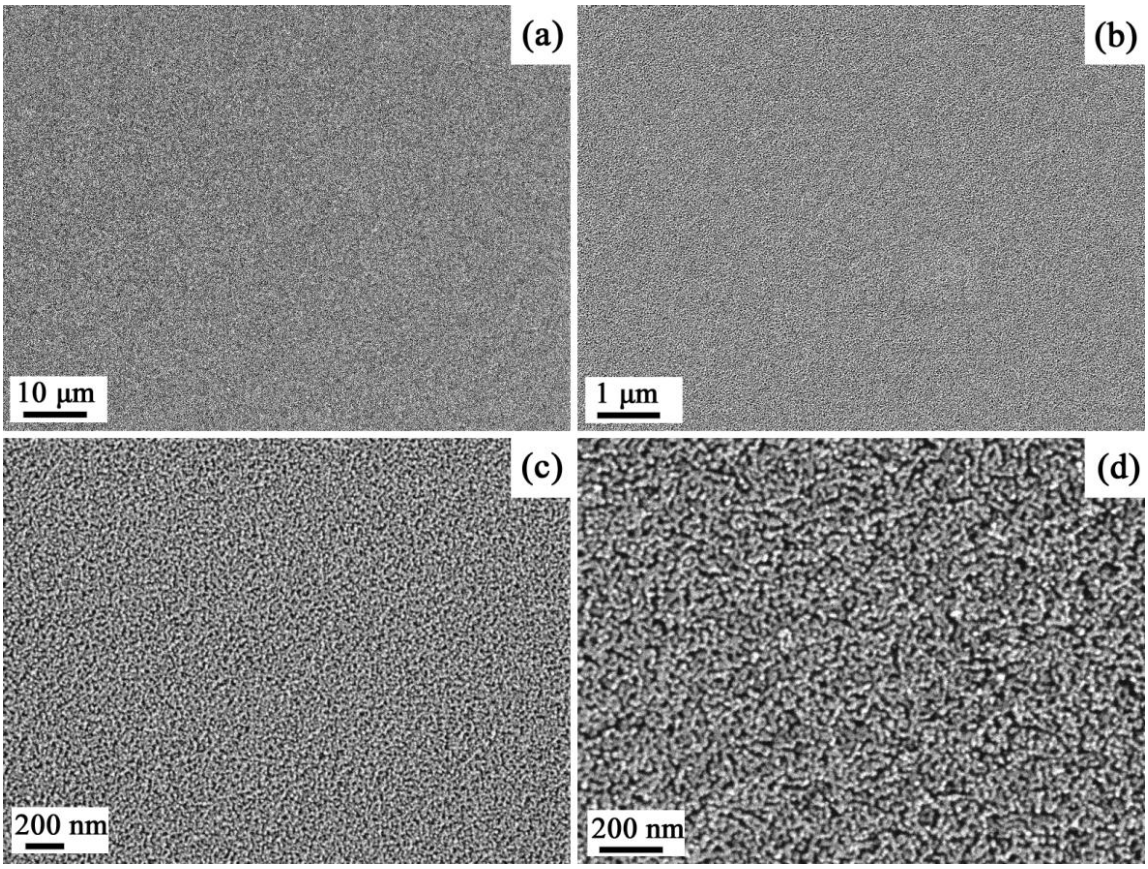

Fig. S1: SEM images of pure SnO_2 mesoporous films at different magnifications.

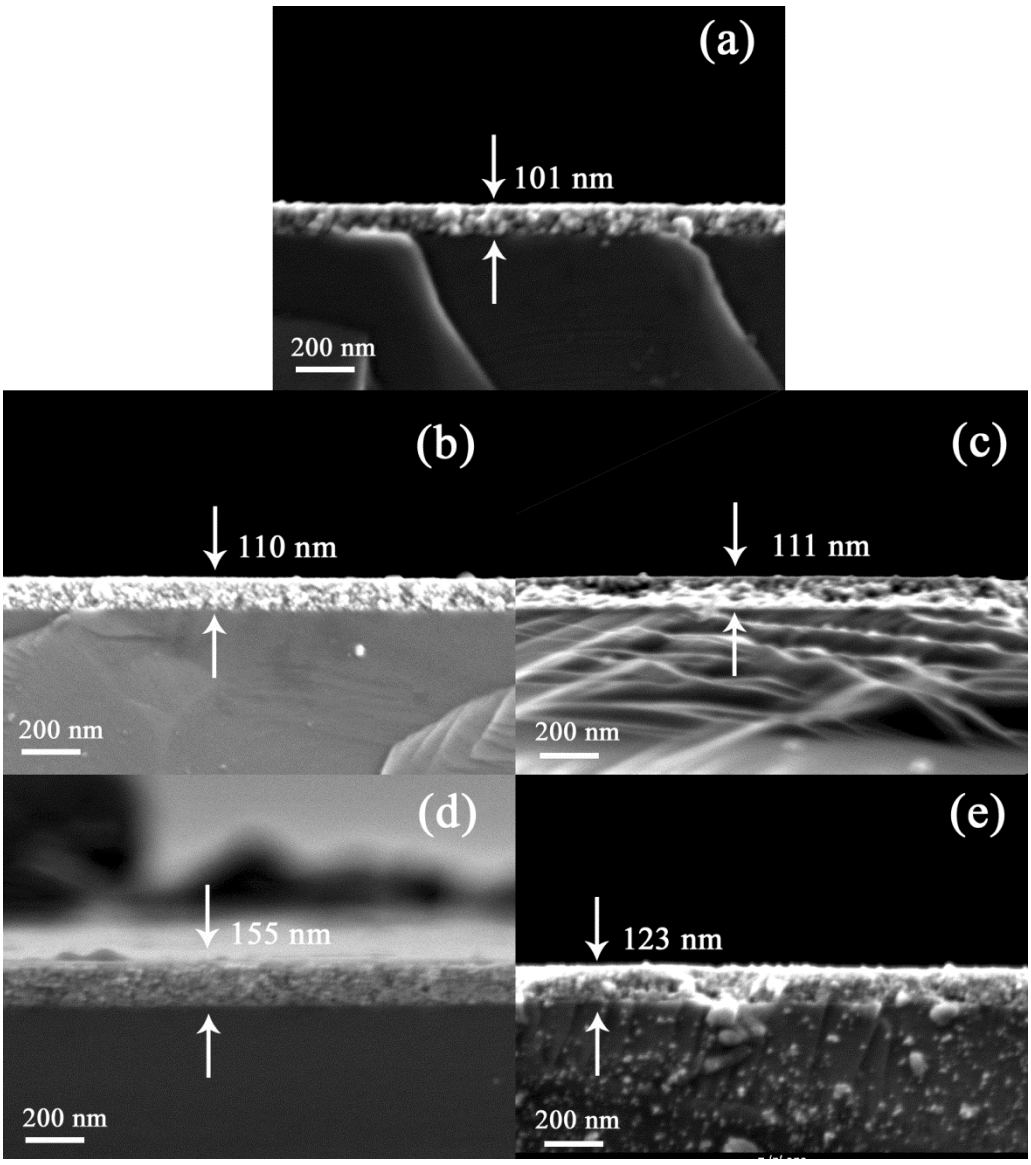

Fig. S2: Cross-section SEM images corresponding to undoped and Ni-doped SnO_2 films synthesized from variable [Ni(II)]/[Sn(IV)] molar ratios: (a) 0:100, (b) 5:95, (c) 10:90, (d) 15:85 and (e) 20:80.

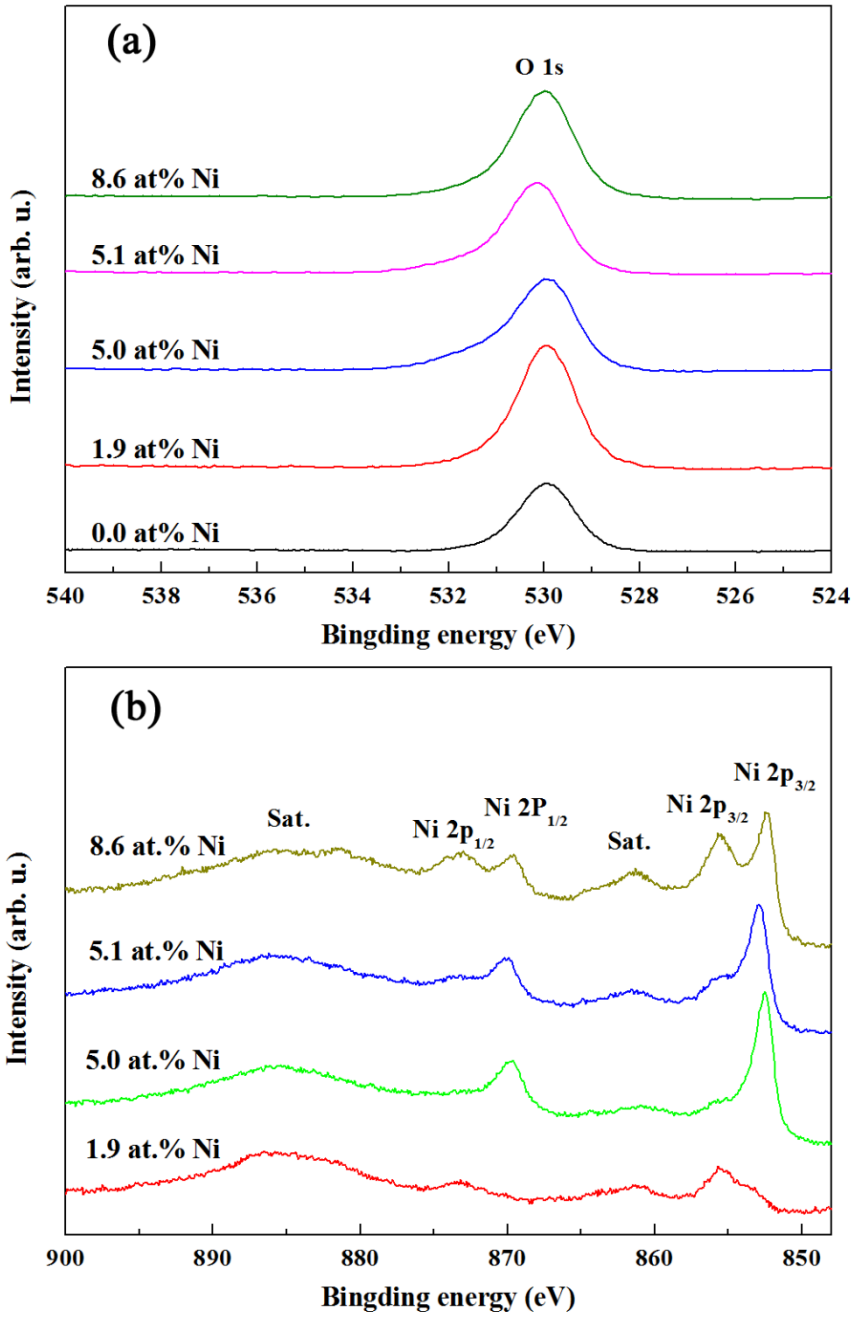

Fig. S3: High resolution XPS spectra of (a) O 1s and (b) Ni 2p for all the investigated samples.

Table of Contents Figure